

Metastable helium in the thermosphere

S. R. KULKARNI¹

¹ Owens Valley Radio Observatory 249-17, California Institute of Technology, Pasadena, CA 91125, USA

(Received Friday 19th September, 2025:00:18)

ABSTRACT

SPHEREx, a recently launched astronomy mission, detected a bright $1.083\text{ }\mu\text{m}$ emission feature in the commissioning data. The PI group attributed this feature to the He I $1.0833\text{ }\mu\text{m}$ triplet line. Here, I review the physics and aeronomy of this well-known line of atmospheric origin. SPHEREx is in a dawn-dusk sun-synchronous polar orbit, circling the earth nearly 15 times a day and observing close to the terminator plane. With a height of 650 km, SPHEREx is located in the upper thermosphere that is dominated by atomic oxygen and helium. The He I line is a result of resonance scattering of solar photons by metastable helium atoms. It appears that SPHEREx has the capacity to provide a rich dataset (global, daily, and 2-minute cadence) of the column density of metastable helium in the upper thermosphere. As an example of this assertion, *with data from just one orbit*, the winter helium bulge was readily seen. Rapid variations in the column density of metastable helium is seen over the south pole, which is probably due to spatial structure in the distribution of metastable helium as well as solar activity. Helium in the thermosphere is of considerable interest to operators of low-earth orbiting (LEO) satellites, since drag in the thermosphere is the primary cause of the decay of these satellites. SPHEREx, along with on-going ground-based studies (passive NIR spectroscopy, lidar, incoherent scatter radar), is poised to contribute to this topic.

1. SPHEREX

On March 12, 2025, SPHEREx¹ was launched into a polar orbit from Vandenberg Space Force Base. The goal of this mission is to image the entire sky in 102 low-resolution “spectrophotometric” bands covering the wavelength range $0.75\text{--}5\text{ }\mu\text{m}$. The planned survey began on May 1, 2025 and amazingly enough, only two months later, calibrated data, available to the astronomical community, started to flow to the NASA/IPAC Infrared Science Archive² (IRSA). New data, with a delay of two months, are added to this archive.

Crill et al. (2020) provides a comprehensive technical description of the mission. Briefly, a 20-cm telescope feeds six HAWAII-2RG detectors (cf. Hall 2011). Each detector, preceded by a linear variable filter, covers a portion of the full wavelength band of the instrument. For instance, “band 1” covers the wavelength

range $0.75\text{--}1.1\text{ }\mu\text{m}$ whilst band 2 covers $1.10\text{--}1.62\text{ }\mu\text{m}$ and so on. Scanning of the sky results in a given sky position sampling different parts of the bandpass. Following in-orbit check-out, the PI team identified a bright spectral line which was seen in all band 1 images with the He I $1.0833\text{ }\mu\text{m}$ triplet. This line has been known to atmospheric scientists through ground-based observations since 1957. In the atmosphere of the earth it arises from resonance scattering of solar photons by helium atoms that are in the $1s2s\text{ }^3S_1$ level. Helium atoms in the $1s2s\text{ }^3S_1$ level decay extremely slowly to the ground state ($1s^2\text{ }^1S_0$), whence the moniker, “metastable” helium.

SPHEREx obtains images in six bands, at a uniform cadence (integration time of 113.6 s). The thermospheric He I intensity data will certainly provide grist for the aeronomer’s mill. Many of my astronomy colleagues have been complaining that this He I line is stymieing their quest to understand the rest of the universe. Some have been tempted to apply AI/ML to predict or minimize the scourge. A modest understanding of the underlying physics and phenomenology provides a strong foundation for building such models. Finally, tyros and neophytes of the interstellar medium (ISM) would benefit from understanding the phenomena and physics of

Corresponding author: S. R. Kulkarni
 srk@astro.caltech.edu

¹ <https://spherex.caltech.edu/>

² <https://www.ipac.caltech.edu/project/irsa>

this important line but in a very different physical setting.

The remainder of this paper is organized as follows. In §2, I summarize the band 1 SPHEREx observations. In §3, I recount the history of metastable helium. This is followed by a brief summary of the use of the principal lines of metastable helium ($1.0833\text{ }\mu\text{m}$ and $\lambda 3889$) in astronomy and aeronomy. In §4 the (astronomical) reader is presented with a summary of the vertical structure of the atmosphere with emphasis on helium. §5 is focused on metastable helium in the thermosphere. The concentration of metastable helium in the thermosphere is determined by a number of processes (the physics of which is well known but the aeronomy of which still constitutes state-of-the-art research). For this reason, the column density of metastable helium in the upper thermosphere (and beyond) is treated as a free parameter (whose value to be determined by observations). In §6, assuming that the primary source of He I photons from resonance scattering of solar photons by metastable helium, I computed the brightness of the He I line(s). Good agreement is found between the calculations and deductions from recent ground-based (lidar) observations. A summary of possible destruction pathways for metastable helium in the upper thermosphere concludes this section. Since the brightness of the He I lines is directly proportional to the intensity of sunlight, it is important that the reader has a clear understanding of the intensity of sunlight along the orbit of SPHEREx. With this in mind, the orbital geometry is summarized in §7. In §8 I present He I line intensity for two full days, centered on the northern solstice (2025 June 20 and 21). The observed strong asymmetry between He I emission in the northern and southern ecliptic poles is attributed to a manifestation of the “winter helium bulge”. Dramatic variations in He I line intensity, on minute timescales, in the south pole region. This is likely a result of spatial variations as well as solar activity. The continuous cadence and comprehensive sampling of the thermosphere close to the day-night terminator plane will result in a unique data set for aeronomers (§9). I conclude this section discussing possible science returns for aeronomy by scheduling observations with ground-based facilities at times of overhead passage of SPHEREx.

Unless otherwise mentioned, all atomic data are from the Atomic Spectrum Database³ of NIST. All wavelengths are in vacuum.

2. THE OBSERVATIONS

³ <https://www.nist.gov/pml/atomic-spectra-database>

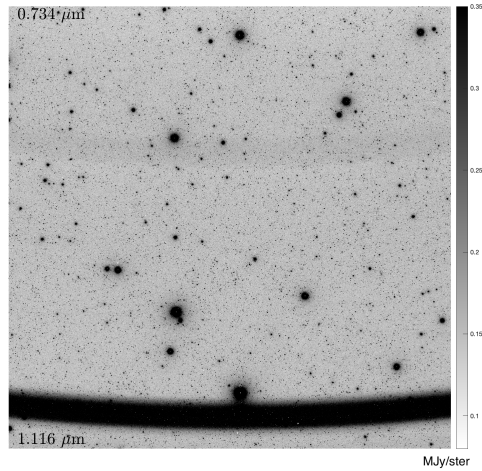


Figure 1. Band 1 image of the sky taken at UT 2025-06-20 00:00:46.9. The image size is $3.5^\circ \times 3.5^\circ$; North is up and East to the left. The pixel values are in MJy/ster and the thermometer (right side) provides the gray-scale mapping to pixel values. The linear variable filter is designed to provide a gradient in the pass-band wavelength in the vertical direction. For this band, as noted in the figure, the passband wavelength at the top is $0.734\text{ }\mu\text{m}$, increasing to $1.116\text{ }\mu\text{m}$ towards the bottom. The unit for the numbers on the (right) vertical thermometer is MJy/ster. The dark slightly curved horizontal band at the bottom of the image is the atmospheric He I $1.0833\text{ }\mu\text{m}$ triplet. The ghostly curved band at $0.85\text{ }\mu\text{m}$ is an artifact (see §A).

The fundamental reference to SPHEREx data is the “Explanatory Supplement”⁴ (hereafter, the *Supplement*) provided by IRSA. Band 1 data were downloaded from IRSA. An example band 1 image is shown in Figure 1. Note the vertical gradient in λ , the passband wavelength. The spectral resolution, $\mathcal{R} = \lambda/\delta\lambda$, is determined by the vertical gradient; here, $\delta\lambda$ is the full width at half-maximum of the linear filter response function for a narrow line. For band 1, $\mathcal{R} = 39$. The bright curved feature at the bottom of the image is centered on $1.083\text{ }\mu\text{m}$ and identified with He I $1.0833\text{ }\mu\text{m}$ triplet. The histogram of the pixel values is presented in Figure 2.

The extraction of the sky spectrum is described in §A. An example sky spectrum is shown in Figure 3. We see that the peak spectral intensity of the He I $1.0833\text{ }\mu\text{m}$ line is $I_\nu \approx 0.23\text{ MJy ster}^{-1}$, brighter than the zodiacal background at $0.15\text{ MJy ster}^{-1}$. The intrinsic width of this triplet is $< 1\text{ \AA}$. The low spectral resolution of the SPHEREx variable linear filter explains the noticeable

⁴ https://irsa.ipac.caltech.edu/data/SPHEREx/docs/SPHEREx_Expsupp_QR_v1.1.pdf

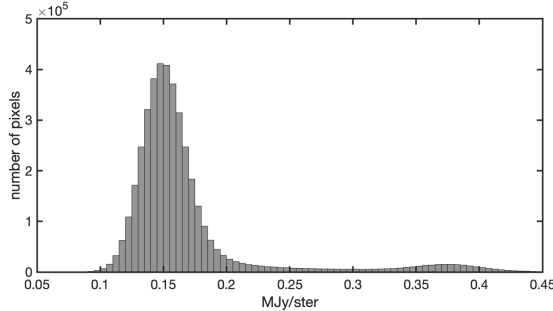


Figure 2. Histogram of the pixel values for the image shown in Figure 1. The zodiacal background is measured by the mode. The secondary hump at $0.38 \text{ MJy ster}^{-1}$ is due to terrestrial He I $1.0833 \mu\text{m}$ emission.

full width at half-maximum of $0.026 \mu\text{m}$ seen in this figure.

For spectral lines, a better choice for intensity is the line-integrated photon intensity, $\mathcal{I} = \int I_\nu / (\hbar\nu) d\nu$, expressed in Rayleigh⁵. This quantity is approximated by $\int I_\nu d\nu / (\hbar\nu_0)$ where ν_0 is the center frequency of the line.

As can be gathered from Figure 3, our data analysis yields $F \equiv \int I_\nu d\lambda$ whose units are $\text{MJy ster}^{-1} \mu\text{m}$. Noting that $|d\lambda| = d\nu(c/\nu^2)$ we find $\mathcal{I} = (a\nu_0) / (c\hbar\alpha)F$ with $a = 10^{-17} \times 10^{-4}$ to convert $\text{MJy ster}^{-1} \mu\text{m}$ to CGS units ($\text{erg cm}^{-2} \text{s}^{-1} \text{Hz}^{-1} \text{ster}^{-1}$) and $\alpha = 10^6/(4\pi)$ to convert CGS to Rayleigh. Putting all this together,

$$\mathcal{I}_{1.0833 \mu\text{m}} = 1.751 \times 10^4 F_{1.0833 \mu\text{m}} R .$$

In Figure 3 we see $F_{1.0833 \mu\text{m}} = 0.006 \text{ MJy ster}^{-1} \mu\text{m}$. Thus, $\mathcal{I}_{1.0833 \mu\text{m}} = 105 R$. For comparison, the zodiacal light is $\mathcal{I}/\mathcal{R} = 138 R$ over spectral width of $\delta\lambda = 0.026 \mu\text{m}$.

3. METASTABLE HELIUM

It was well known to the early atomic physicists that helium, unlike hydrogen, exhibited two sets of lines. These were empirically attributed to “para-helium” and “ortho-helium”. Their origin was not understandable in the “old” quantum theory of Bohr & Sommerfeld. In 1926, Heisenberg, with his “new quantum” theory, provided the modern explanation, namely that helium has two spectroscopic families: singlet ($S = 0$) and triplet ($S = 1$). We now know that transitions across the spin families are not allowed (“semi-forbidden”) which explains the observed distinct families.

The lowest level of para-helium is $1s^2 1S_0$ (the true ground state), while that for ortho-helium is $1s2s 3S_1$.

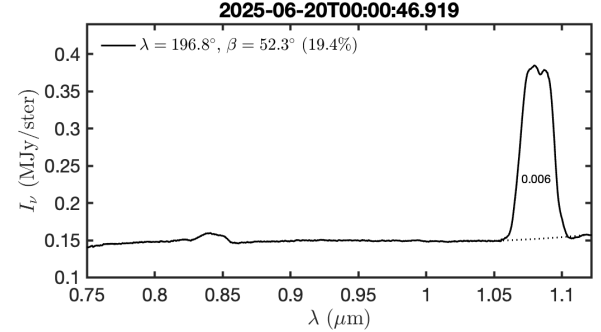


Figure 3. Sky-spectrum (solid black line) of band 1 image shown in Figure 1. The He I triplet is the bright feature at the right end of the spectrum. The dotted black line is the baseline constructed from the wavelength range $[1.02, 1.05] \mu\text{m}$ and $[1.115, 1.16] \mu\text{m}$. The full-width at half-maximum of the He I line is found to be $0.026 \mu\text{m}$, which is in accord with the pre-launch specifications for the instrument (Crill et al. 2020). F , the integral of the intensity over the line (unit: $\text{MJy ster}^{-1} \mu\text{m}$), is noted above the black dotted line. The geo-centric ecliptic longitude (λ) and latitude (β) of the bore-sight are noted in the legend. Also included in the legend is the percentage pixels rejected in the image frame (see §A). The sun-earth(center)-satellite angle, at the start of the observation (shown in title as UT time) is 76° and the sun-earth(center)-bore-sight angle is 97° . The integration time is 113.6 s. The dimple in the middle of the He I line is an artifact anticipated from pre-flight model and the small bump at $0.85 \mu\text{m}$ is due to the ghost feature seen in Figure 1 and discussed in the caption to that figure.

A simplified Grotrian diagram is presented in Figure 4. The lifetime of ortho-helium in the lowest state is A_*^{-1} where A_* is the A-coefficient of the semi-forbidden $1s2s 3S_1 \rightarrow 1s^2 1S_0$ transition. The modern value for A_*^{-1} is about 2.2 hours, an eternity for permitted transitions. For this reason, helium in the $1s2s 3S_1$ state is called metastable helium. In atomic physics, metastable helium is sometimes labeled ${}^4\text{He}^*$.

Metastable helium is long-lived enough to open up all sorts of interesting phenomena. For example, ${}^4\text{He}^*$ is magnetic (Pancharatnam 1968), unlike ${}^4\text{He}$. Due to the high internal energy ${}^4\text{He}^*$ is used for QED precision tests. The bosonic nature opens up novel tests of quantum optics (see Abbas et al. 2021). Bosonic ${}^4\text{He}^*$ and fermionic ${}^3\text{He}^*$ allow novel studies of Bose-Fermi mixtures (Thomas et al. 2023). Finally, it is the metastable state of both He and Ne that lies at the heart of He-Ne lasers.

Returning to the topic at hand: the He I $1.0833 \mu\text{m}$ line results from $1s3p 3P \rightarrow 1s2s 3S_1$. Historically, in astronomy, the blue optical triplet $\lambda 3889 \text{ \AA}$ ($1s4p 3P \rightarrow 1s2s 3S_1$) was observed first. These lines are shown in Figure 4 and the relevant atomic data are summarized in Table 1.

⁵ 1 Rayleigh or $R = 10^6/(4\pi) \text{ phot cm}^{-2} \text{s}^{-1} \text{ ster}^{-1}$ is the traditional unit for surface brightness in the fields of aeronomy and the study of diffuse ionized gas in the Milky Way.

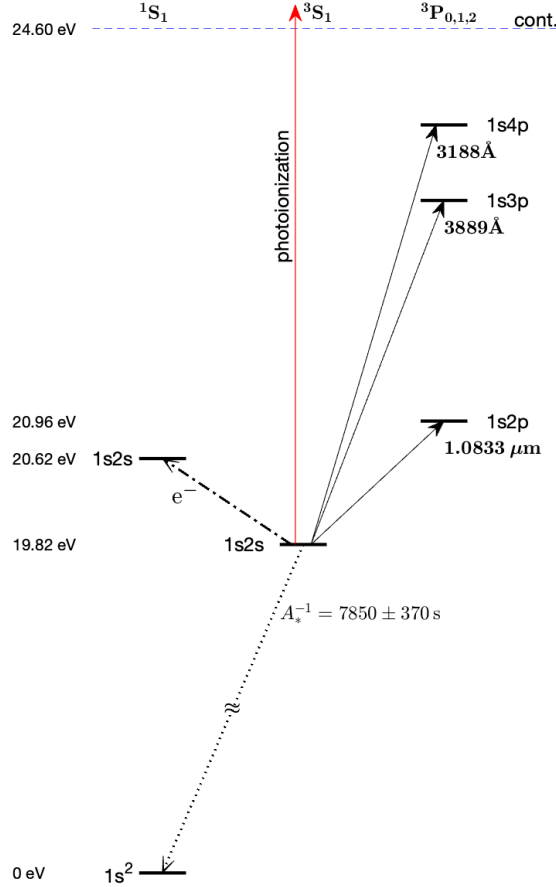


Figure 4. Simplified Grotrian diagram for He I with focus on metastable helium. The energy scale (left side), apart from a break (indicated by \approx sign) between the ground state and the metastable level, $1s2s\ ^3S_1$, is linear. Key allowed transitions of the metastable level are shown by solid lines. The semi-forbidden decay from $1s2s\ ^3S_1$ to the ground state, with small A-coefficient, is shown by the dotted line. Collisions with electrons can excite atom to $1s2s\ ^1S_1$ (labeled, e^-) or $1s2p\ ^3P$ level (not labeled to avoid clutter) and can also de-excite metastable helium to ground state (not labeled). Photons with energy > 4.768 eV have the capacity to photoionize metastable helium (red line).

3.1. A brief history of A_*

Astronomers starting with Viktor Ambartsumian in the thirties were aware of the possible diagnostic value afforded by metastable helium. However, in those early days, even the mode of decay (two-photon versus magnetic dipole) was not known, let alone a rough value for A_* . Goldberg (1939) attributed the brightness of the optical lines of the triplet family relative to those of the singlet family, in the solar corona, to the “metastability” of the 3S_1 level. The line became a mainstay of solar research (e.g., Zirin & Dietz 1963) and, given its ability to trace the chromosphere and outflow, was applied to study active stars (e.g., Zirin 1976).

Table 1. Two major triplets of metastable He

| λ (nm) | u | A_{ul} (s^{-1}) | f_{lu} |
|----------------|-----------------|-----------------------|----------|
| 1,083.205 7482 | $1s2p\ ^3P_0^o$ | 1.02×10^7 | 0.0599 |
| 1,083.321 6761 | $^3P_1^o$ | ” | 0.1796 |
| 1,083.330 6454 | $^3P_2^o$ | ” | 0.2994 |
| 388.970 65567 | $1s3p\ ^3P_0^o$ | 9.47×10^6 | 0.0072 |
| 388.974 75124 | $^3P_1^o$ | ” | 0.0215 |
| 388.975 08392 | $^3P_2^o$ | ” | 0.0358 |

NOTE— λ is the wavelength of the transition. u is the upper state. For the lines listed here, the lower state (l) is $1s2s\ ^3S_1$. A_{ul} is the A-coefficient of the ul transition and f_{lu} is the corresponding oscillator strength. The sum of the oscillator strengths for the triplet $1.0833\ \mu m$ line is 0.5389 and 0.0645 for the $3889\ \text{\AA}$ triplet. The sum of the oscillator for all the allowed transitions from $1s2s\ ^3S_1$ up to $1s10s$ is 0.66. The effective wavelength for each triplet, calculated by weighting the transition wavelengths by g_u (the degeneracy of the upper state), is 1083.3138 nm and 388.9745 nm.

Mathis (1957), assuming two photon decay, estimated a value of $A_* = 2 \times 10^{-5}\ s^{-1}$. Drake & Dalgarno (1968) showed an error in this calculation and revised the estimate to $< 4 \times 10^{-9}\ s^{-1}$ (Drake et al. 1969). The small value of A_* raised the exciting possibility of a detectable population of metastable helium in astronomical settings. Rees, Sciama & Stobbs (1968) extended the calculations to include optical absorption from cluster gas and the intergalactic medium⁶ while Scherb (1968) called for observations of Galactic ISM in the $1.0833\ \text{nm}$ line.

By 1970s QED calculations became possible and it became immediately clear that the magnetic dipole (M1) interaction dominates over two-photon decay (cf. Drake 1971). Experimental measurements carried out two years later found $A_* \approx 2.3 \times 10^{-4}\ s^{-1}$ with an error of a third of the value (Moos & Woodworth 1973). Currently, the best experimental measurement value is $A_* = (1.274 \pm 0.06) \times 10^{-4}\ s^{-1}$ which corresponds to A_*^{-1} of $7850 \pm 370\ s$ (Hodgman et al. 2009; see this article for a history of QED calculations of A_*).

3.2. Line(s) of metastable helium: Astronomy

The first detection of metastable helium⁷ seems to be by Adams (1949). Indriolo et al. (2009) and Galazutdinov & Krelowski (2012) revisited the same topic (Galac-

⁶ The article ends with the statement that 1-photon decay calculations were on the verge of being carried out and this channel was likely to be faster than the 2-photon decay channel.

⁷ Absorption of the $1s2s\ ^3S_1 \rightarrow 1s4p\ ^3P_{0,1,2}$ $\lambda 3888\ \text{\AA}$ triplet

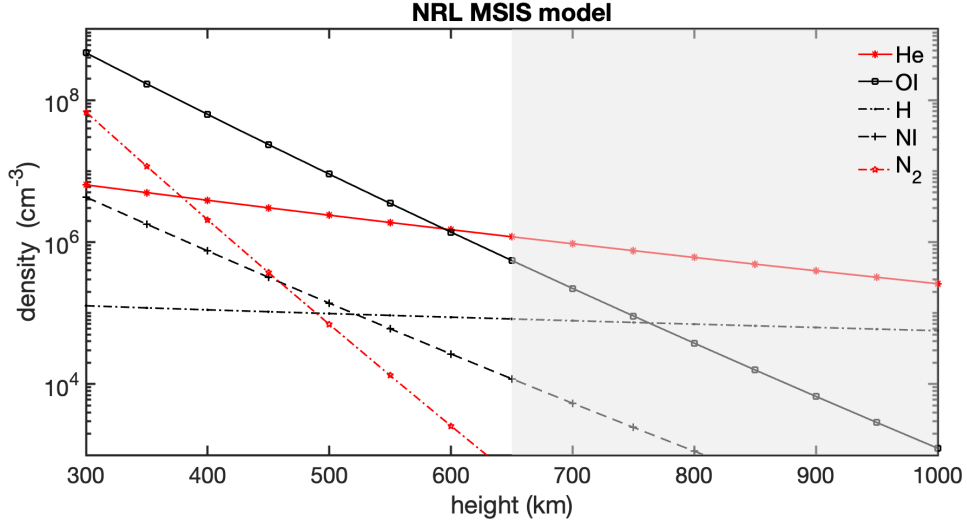


Figure 5. Naval Research Laboratory (NRL) Mass Spectrometer and Incoherent Scatter radar (MSIS) model of the neutral species in the upper atmosphere for a location defined by terrestrial longitude of $\lambda = 90^\circ$ and terrestrial latitude of $\phi = 30^\circ$ on UT 2025 June 20 at 12:00 am. Throughout the thermosphere, the temperature of the neutral species is about 1100 K. The atmosphere above the orbit of SPHEREx (height, 650 km) is shown in gray. The model data were generated using NRLMSIS 2.0 (<https://ccmc.gsfc.nasa.gov/models/NRLMSIS~2.0/>).

tic ISM) but with the He I 1.0833 μm line instead. As noted by solar astronomers, lines of metastable helium, can trace the transition from outflow to winds (Ulrich & Wood 1981; Dupree et al. 1992) and, as such, has been pressed in the study of young stars with inflows and outflows (e.g. Edwards et al. 2003), of giant stars stars (Dupree et al. 2009) and R Corona Borealis stars (Clayton et al. 2013). The line has also been used in the study of explosive and / or energetic phenomena: galactic nuclei (Anderson & Kraft 1969), classical novae (Naito et al. 2013), and tidal disruption events (Hung et al. 2019). In exoplanets, investigations of He I 1.0833 μm began in 2018 (Oklopčić & Hirata 2018; Spake et al. 2018). This diagnostic has now transitioned from a cottage industry to an industrial operation.

3.3. Line(s) of metastable helium: Aeronomy

During the day, the He I 1.0833 μm line is as bright as 15 kilo Rayleigh (kR); see, for example, Harrison & Cairns (1969). In the terrestrial context, it was first discovered by observations taken at Moscow in 1957, following a particularly strong auroral storm⁸ (see Shefov 1964 and the references therein). However, most of the ground-based observations were made after the sun set or before the sun rose to avoid Rayleigh scattering from the sun. Once the thermosphere is no longer illuminated by sunlight, the line disappears and so the usable time is restricted to SZA, less than, say, 130° ; here SZA is

the zenith angle of the sun (with 90° corresponding to sunset or sunrise). The underlying physics for the production of metastable helium in the thermosphere was developed and clarified by Bishop & Link (1993). The further discussion of this topic is postponed to §4.

4. HELIUM IN THE ATMOSPHERE

At sea level, in the dry atmosphere, helium, with an abundance of 5.24 ppm (parts per million), is the sixth most abundant species after N, O, Ar, CO₂ and Ne. This is followed by Kr, SO₂ and CH₄ (> 1 ppm). Other trace species such as H₂, Xe, O₃, NO₂, I₂ and CO and NH₃ have abundances below 1 ppm. The low concentration of helium makes commercial extraction of helium from the air impractical. Instead, it is obtained as a by-product of the extraction of natural gas.

The working hypothesis is that helium in the atmosphere originates from the decay of radioactive elements (particularly, uranium and thorium). The outgassing of helium from the crust is estimated to be $2 \times 10^6 \text{ atom cm}^{-2} \text{ s}^{-1}$ (MacDonald 1963). In recent times, as a consequence of the increased extraction of natural gas, the concentration of both ⁴He (and, surprisingly, ³He) has been gradually increasing (Birner et al. 2022).

For the astronomers, I provide a short summary of the vertical structure of the atmosphere. The lowest level is the troposphere [0–10 km] in which, as we know from experience, the temperature falls with height; the stratosphere [10–50 km] where, due to heating provided by solar photo-dissociation of ozone, the temperature

⁸ Coincidentally, the International Geophysical Year, IGY, began in July 1957.

gradient is reversed; the mesosphere [50–80 km] where the temperature gradient becomes negative again; the thermosphere [80–600 km] where the temperature gradient becomes positive again due to heating provided by solar photo-dissociation of O₂; and finally the exosphere, which depending on solar activity, variously starts at 600 km to 1,000 km.

The run of dominant neutral species in the altitude range of interest for SPHEREx is shown in Figure 5. It is interesting to note that the dominance of helium at the top edge of the thermosphere was first inferred by orbital decay of the Echo 1 “balloon-satellite” (Nicolet 1961). For neutral species, the highest temperatures in the thermosphere range from 1,000 K to 2,000 K (depending on solar activity). Above about 1,000 km, the atmosphere becomes a gentle wind that carries the lightest elements (H, He)– the exosphere.

The loss of helium from the earth’s atmosphere is an important problem in Earth science. MacDonald (1963) and Kockarts (1973), although dated, are good starting points while Hunten (1982) provides an overview of outgassing of the planets (including earth) of the solar system. Briefly, the earth loses hydrogen and helium as a result of three processes. These are (i) Jean’s escape (fast moving particles on the Maxwellian tail escape the earth), (ii) charge exchange of an atmospheric helium atom with energetic solar protons, and (iii) polar wind escape (acceleration of ions along open field lines at the magnetic poles). Currently, it is estimated that the earth loses 3 kg s⁻¹ of hydrogen and 50 g s⁻¹ of helium (Catling & Zahnle 2009). All three processes discussed above are sensitive to the activity of the sun. The orbital longevity of low earth orbit (LEO) satellites is sensitive to the expansion and contraction of the thermosphere.

5. METASTABLE HELIUM IN THE THERMOSPHERE

In aeronomy, it appears that Bishop & Link (1993) is considered the defining document of all relevant theoretical processes with respect to the intensity of the He I 1.0833 μ m line. Waldrop et al. (2005) present an analysis of a comprehensive (radar and Fabry-Pérot) year-long program at the Arecibo Observatory aimed at studying metastable helium.

In the thermosphere, a number of processes can produce metastable helium: collisional excitation with energetic electrons, recombinations with low energy electrons and (successive) charge exchange of fast moving alpha particles in the solar wind plowing into the thermosphere (see, for example, Reasoner 1973). However, the dominant process is collisional excitation by freshly minted photoelectrons (see Bishop & Link 1993). Such

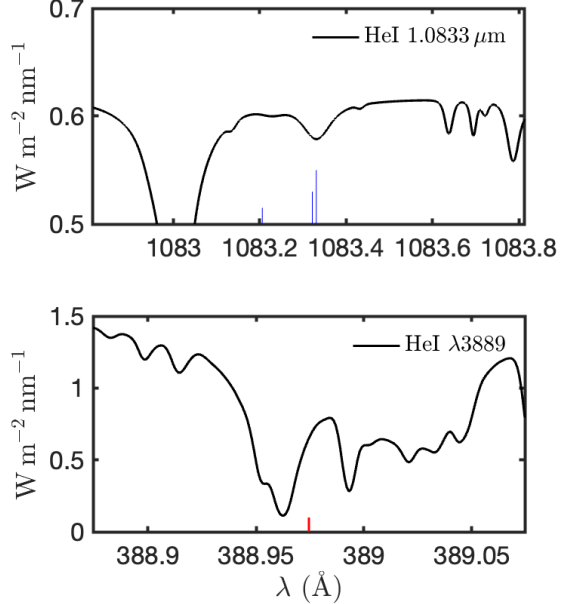


Figure 6. Zoom-in of the TSIS-1 HSRS solar spectrum centered on wavelengths of He I 1.0833 μ m and He I λ 3889. For the 1.0833 μ m line, vertical blue stubs mark the three lines with height proportional to strength. For λ 3889 the red vertical stub marks the effective wavelength of the triplet (see notes to Table 1). The data were obtained from https://lasp.colorado.edu/lisird/data/tsis1_hsrs_p1nm; see Coddington et al. (2023) for further details.

energetic electrons are produced by molecules and/or atoms that absorb solar EUV photons.

The destructive pathways for metastable helium, other than radiative decay to the ground state, are as follows: photoionization, electron collisional de-excitation to the ground state, and electron collisional excitations to singlet levels, especially adjacent energy levels (e.g., 1s2s ¹S₀, 0.79 eV above 1s2s ³S₁; 1s2p ¹P₀, 1.4 eV above) which then undergo rapid radiative decay. These processes are illustrated in Figure 4. In the upper thermosphere, photoionization by sunlight is important whereas below 350 km, Penning ionization⁹ is very effective in suppressing metastable helium.

Here, we treat the column density of metastable helium above the orbit of SPHEREx as a free parameter whose value would be determined from the SPHEREx observations. The proposed model for the origin of the He I line is simple: the source of 1.0833 μ m emission is

⁹ Collisions of the sort He^{*}+X where X is another species result in ionization of X. In this context, X is O₂, N₂, O⁰ and H⁰. This process, discovered by F. M. Penning of Philips Natuurkundig Laboratorium, Eindhoven, Netherlands, is the key mechanism that underlies the operation of house-hold tube lights.

primarily due to resonance scattering of solar photons by metastable helium.

6. RESONANCE SCATTERING OF SOLAR PHOTONS

Our goal is to compute the absorption cross section for the lines of interest. We start the exercise by noting that the thermal broadening of the helium atoms, $\sigma_v \approx 1.4T_3^{1/2} \text{ km s}^{-1}$, is small, as are the wind velocities in the thermosphere; here, $T = 10^3 T_3 \text{ K}$ is temperature of the helium gas. For the “top of the atmosphere” solar spectrum, we elected to use the “Total Spectral Solar Irradiance Sensor-1 Hybrid Solar Reference Spectrum” (TSIS-1 HSRS; Coddington et al. 2021, 2023) because of its higher spectral resolution (0.01 nm) relative to SOLSPEC (which ranges from 0.6 to 9.5 nm; Meftah et al. 2018).

The solar spectrum in the vicinity of the $1.0833 \mu\text{m}$ line and the $\lambda 3889$ line is shown in Figure 6. The spectral flux density at $1.0833 \mu\text{m}$ is $f_\lambda = 0.58 \text{ W m}^{-2} \text{ s}^{-1} \text{ nm}^{-1}$ which translates to $2.27 \times 10^{-9} \text{ erg cm}^{-2} \text{ s}^{-1} \text{ Hz}^{-1}$ or $N_\nu(0) = 1.24 \times 10^3 \text{ phot cm}^{-2} \text{ s}^{-1} \text{ Hz}^{-1}$.

The absorption cross-section is

$$\sigma_{lu}(\nu) = \frac{\pi e^2}{m_e c} f_{lu} \phi_\nu$$

where f_{lu} is the oscillator strength (see Table 1), $\phi(\nu)d\nu$ is the probability of photon being observed over the interval, $[\nu, \nu+d\nu]$ and $\int \phi_\nu d\nu = 1$. The optical depths are small, so we can ignore the damping wings. Metastable helium can be excited to any of the three levels of ${}^3\text{P}_{0,1,2}$. At the spectral resolution of relevance to this paper the resulting lines are at the same wavelength. So, what matters is the sum of the three oscillator strengths. The scattering rate per atom is simply $\mathcal{R}_{1.0833} = (\pi e^2 / m_e c) f_{^3\text{S}_1 \rightarrow {}^3\text{P}_{0,1,2}} N_\nu(0) = 17.7 \text{ phot atom s}^{-1}$.

The photon intensity of the scattered $1.0833 \mu\text{m}$ line is given by $n_{\text{He}^*} L \mathcal{R}_{1.0833} / (4\pi)$ where n_{He^*} is the number density of metastable helium and L is the length of the column of metastable helium. Normalizing to a path length of 100 km we find

$$\mathcal{I}_{1.0833} = 177 n_{\text{He}^*} L_2 R. \quad (1)$$

where $L_2 = L / (100 \text{ km})$ and n_{He^*} is in cm^{-3} .

A similar exercise can be carried out for the 3889 \AA triplet (Table 1). The spectral flux density at this wavelength is $0.56 \text{ W m}^{-2} \text{ nm}^{-1}$. The corresponding scattered-photon intensity is

$$\mathcal{I}_{3889} = 0.95 n_{\text{He}^*} L_2 R.$$

6.1. Expectations

In this subsection, we confront our model expectations with existing data and accepted models for metastable helium in the thermosphere.

A recent development in aeronomy has been the use of lidar: shining a bright beam at a wavelength of $1.0833 \mu\text{m}$ into the thermosphere. Currently, there are two facilities: Deutsches Zentrum für Luft- und Raumfahrt (DLR; German Aerospace Center; Munich; $48^\circ \text{N}, 11^\circ \text{E}$; Kaifler et al. 2022) and the Chinese Meridian Project group operating from Danzhou, Hainan Province, China ($19.5^\circ \text{N}, 109^\circ \text{E}$; Zhao et al. 2024). The DLR group conducted measurements during the northern winter period, when the intensity of $\text{He I } 1.0833 \mu\text{m}$ is expected to be the brightest (Geach & Kaifler 2025). The inferred densities for metastable helium were a few atom cm^{-3} . Putting this density in Equation 1 we find intensities approaching 1 kR that match the highs seen in Figure 10. Separately, if the typical density of metastable helium atoms is 1 cm^{-3} , then from Figure 5, we see that the fractional abundance of metastable helium is very small $\lesssim 10^{-6}$.

6.2. Photoionization

In the upper thermosphere, the primary process for the destruction of metastable helium is photoionization (Bishop & Link 1993). The ionization potential of metastable helium is $\text{IP}=4.768 \text{ eV}$ (see Figure 4) corresponding to $\lambda = 2600 \text{ \AA}$. Incidentally, recently, $\nu_{\text{ip}} = \text{IP}/h$ has been measured with high precision, $1, 152, 842, 742.7082(55) \text{ MHz}$ (Clausen et al. 2025). This value appears to be in discrepancy with the best QED calculations (Patkóš et al. 2021) by 9σ .

The photo-ionization rate per metastable atom is $\mathcal{R}_{\text{pi}} = \int_{\nu_{\text{pi}}}^{\infty} f_\nu / (h\nu) \sigma_{\text{pi}}(\nu) d\nu$, where $\sigma_{\text{pi}}(\nu)$ is the bound-free cross-section at frequency, ν , and $f_\nu = \lambda f_\lambda / \nu$ is the solar spectral flux density. For this calculation high spectral resolution is not needed. In view of this, for the solar intensity spectrum, we elect to use the SOLSPEC spectrum (Meftah et al. 2018).

In §C.1 we summarize the history of improvements in the calculation of σ_{pi} . There we noted that the experimental data lie above the calculation of Norcross (1971) and below that of Del Zanna et al. (2020). The corresponding values for \mathcal{R}_{pi} are $1.4 \times 10^{-3} \text{ s}^{-1}$ and $2.7 \times 10^{-3} \text{ s}^{-1}$, respectively. We adopt the average, $\mathcal{R}_{\text{pi}} \approx 2 \times 10^{-3} \text{ s}^{-1}$, in excellent agreement with Bishop & Link (1993).

6.3. Other processes

For completeness, we now investigate other processes that involve metastable helium. In order not to dis-

tract the reader from the primary focus of the paper, the background of the secondary processes is summarized in §C.2. The run of ion densities is shown in Figure 7 while the run of electron density and temperature(s) can be found in Figure 8. The (astronomical) reader may be surprised to learn that the ionosphere is mildly ionized, with ionization fraction typically less than 1%. Furthermore, as is clear from Figure 8, each species (neutrals, ions, protons, ions) have their own temperatures – a situation not routinely encountered in studies of the interstellar medium.

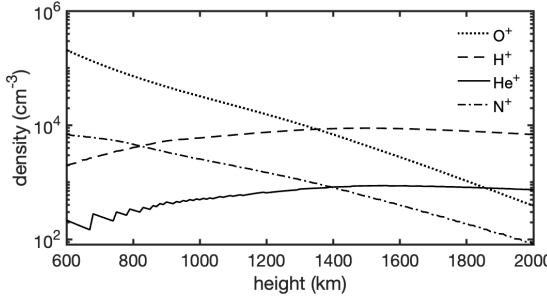


Figure 7. Run of densities of dominant ions with height at terrestrial coordinates: $\phi = 30^\circ$, $\lambda = 90^\circ$ at UT 2025-June-20, 12 noon. The data were obtained by running IRI-2020 (<https://kauai.ccmc.gsfc.nasa.gov/instantrun/iri/>) hosted by International Reference Ionosphere (<https://irimodel.org/>).

First, we investigate the production of metastable helium by recombination. Three quarters of the recombinations will proceed via the triplet ladder, with all ending in $1s2s\ ^3S_1$. In other words, three-quarters of the recombinations result in metastable helium. We adopt an electron density, $n_e = 10^5 \text{ cm}^{-3}$ and an electron temperature of 3,000 K (Figure 8). Applying Equation C1 we find the recombination timescale to be $t_r = (3/4n_e\alpha)^{-1} \approx 1.6 \times 10^7 \text{ s}$.

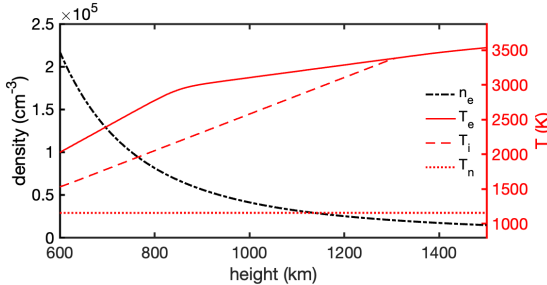


Figure 8. The run of electron density and temperature(s) with height. See caption to Figure 7 for details of the model.

Given Figure 5 we restrict the discussion of Penning ionization of hydrogen atoms by metastable helium. For this endothermic reaction, the rate coefficient, over

a wide temperature range, is $Q = 5 \times 10^{-10} \text{ cm}^3 \text{ s}^{-1}$ (§C.2). From Figure 5 we see that $n_H \approx 10^5 \text{ cm}^{-3}$, over a wide range of altitude. The timescale for the reaction is $(n_H Q)^{-1} \approx 2 \times 10^4 \text{ s}$, much slower than that for photoionization. The density of neutrals increases with decreasing height, whereas solar photoionization remains the same. This calculation shows why at lower heights Penning ionization limits the density of metastable helium atoms.

We finally consider collisions with electrons. The rate coefficient for excitation to the $1s2s\ ^3P$ state is $q = 0.46 \times 10^{-8} \text{ cm}^3 \text{ s}^{-1}$ while $q = 0.76 \times 10^{-8} \text{ cm}^3 \text{ s}^{-1}$ for $1s2s\ ^1S_1$ and $q = 0.23 \times 10^{-8} \text{ cm}^3 \text{ s}^{-1}$ for de-excitation to the ground state. Given $n_e \approx 10^5 \text{ cm}^{-3}$, these timescales are of the order of 10^3 s , a factor of two longer than the photo-ionization timescale. Separately, note that the production of $1.0833 \mu\text{m}$ photons by electron collisional excitation simply does not compete with resonance scattering of solar photons.

7. ORBITAL GEOMETRY

In the framework adopted here, the brightness of the He I line is proportional to the product of the intensity of the incident sunlight and the column density of metastable helium atoms. Changes in either quantity will affect the brightness of the line. Thus, it is important to have a complete understanding of the geometry of the situation before interpreting the data.

The orbit of SPHEREx is almost a circle with a planned semi-major axis of 7037 km and an inclination¹⁰ of 97.95° . In Figure 9, I present the geometry of the orbit of SPHEREx relative to earth and the sun at the northern solstice (UT 2025, June 20).

There are four reference frames: the geocentric ecliptic coordinate system (longitude: λ , latitude: β), the celestial (equatorial) frame (right ascension: α and declination: δ), a frame defined by the magnetic field of the earth and the geographical frame (longitude: λ , latitude: ϕ). Astronomers prefer α and δ . The most natural coordinate system for SPHEREx is the geocentric ecliptic frame because in this frame the orbital orientation is fixed with respect to the sun. Atmospheric scientists naturally prefer the geographical frame. For charged particles, the most natural frame is the terrestrial geomagnetic frame!

¹⁰ The inclination of a satellite orbiting the earth is the angle between orbital plane of the satellite and earth's equatorial plane. A satellite orbiting in the equatorial plane with motion in the same direction of earth's rotation (prograde) has an inclination of 0° . A satellite passing over both poles has an inclination of 90° . A satellite in an equatorial orbit but with motion opposed to earth's motion (retrograde) has an inclination of 180° .

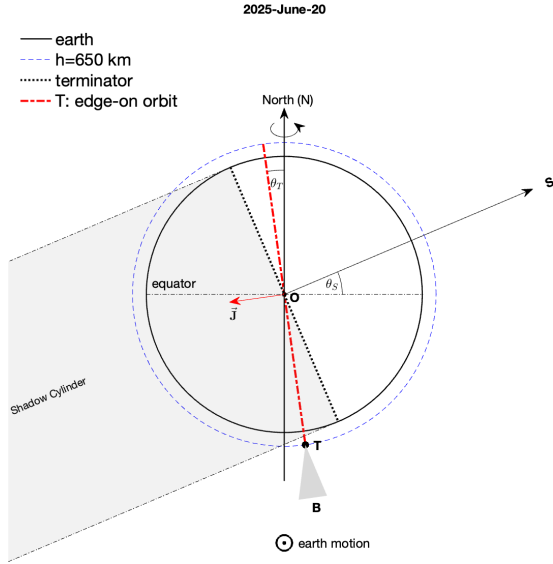


Figure 9. The edge-on orbit of SPHEREx (tilted dash-dotted red line) at the northern solstice (20th June, 2025). SPHEREx is labeled by “T”. The large black circle represents the earth with the celestial north pole marked and the sense of earth’s rotation clearly indicated. The dashed blue curve marks a circle whose height above the earth’s surface is 650 km. The center of the sun (“S”) and the center of earth (“O”) lie in the plane of the paper. Our view is one of looking back at earth from autumnal equinox (first point of Libra). [In regard to the symbol \odot found at the bottom of the figure: we follow the convention of magnetostatics and use the symbol \odot to indicate a vector coming out of the paper. Here, the vector under consideration is the velocity of earth around the sun.] The sun bears an angle, $\theta_S \approx 23^\circ$ with respect to the equatorial plane. The orbit of SPHEREx is tilted with respect to the celestial north pole, $\theta_T \approx 8^\circ$. The angular momentum vector of the orbit of SPHEREx is marked by a thin red arrow (and labeled as \vec{J}). Notice that the east-west velocity component of SPHEREx is retrograde with respect to the rotation of earth. There is an additional angle – the direction of the bore-sight (B) with respect to geocentric radial vector of the orbit of the satellite. This angle is under the control of the project. For illustrative purpose, the range in the choice of this angle is shown by a cone with a half-opening angle of 15° . In the text, we refer to two angles: SOT and SOB. As can be gathered from the labels in this figure, these angles are defined by sun-earth(center)-satellite and sun-earth(center)-boresight.

The reader has no choice but to skip around the frames as and when it makes sense. In this paper, I will be using λ and β because those values are included in the FITS header. As and when needed I compute quantities such as the position of the sun and the sun-earth(center)-satellite, traditionally called the SOT angle (defined and explained in Figure 9) and also the sun-earth(center)-boresight (“SOB”) angle. For example, for the observation presented in Figure 3, SOT= 76° whilst SOB= 97° .

Finally, unless otherwise stated, the term “pole” or “polar” regions refers to the geographical pole.

8. VARIATIONS IN THE HE I LINE

About every two minutes SPHEREx produces images in each of the six bands. I have analyzed band 1 images for two full days that overlap the summer solstice (2025 June 20 and 21). The resulting line-integrated photon intensity of the He $1.0833\ \mu\text{m}$ for these two days is shown in Figure 10. Clearly, the $1.0833\ \mu\text{m}$ emission is periodic. The orbital period of the satellite clearly emerges from a Lomb-Scargle analysis of the light curve (§B).

As noted in the caption of Figure 3, the geocentric ecliptic latitude (λ) and longitude (β) of the bore-sight direction are included in the FITS header. From Figure 10 we see that the He line is strongest at the South Ecliptic Pole (SEP) and weakest when the satellite is pointing towards the region of the North Ecliptic Pole (NEP).

We expect the SOT angle to vary between $90 + \theta_S - \theta_T = 105^\circ$ (which will happen when the satellite is closest to SEP) and $90 - \theta_S + \theta_T = 75^\circ$ (which will happen when the satellite is closest to the NEP). I used JPL’s Horizons system¹¹ to compute SOT for SPHEREx. For June 20, 2025, I find that SOT varies from 75° to 105° . The times of maximum SOT are marked in Figure 10. The match between maximum SOT and peak He I emission means that the emission is the highest in the vicinity of the south polar region.

As can be concluded from Figure 9, the intensity of the solar light at SPHEREx remains unchanged during its orbit. Furthermore, recall that the SPHEREx observes close to the terminator plane. Thus, *we are forced to conclude that, at the northern solstice, the column density of metastable helium in the upper thermosphere is much higher in the south pole region relative to the north pole and the equatorial regions.*

8.1. The winter helium bulge

Persuaded by the striking trend seen in Figure 10, namely an increased column density of metastable helium at the south pole (during northern summer), I perused the aeronomy literature and found considerable literature on the “winter helium bulge” – a notable increase of the concentration of helium in the winter hemisphere of the thermosphere relative to the summer hemisphere. This effect was discovered in 1968 by G. Keating and E. Prior using satellite drag measurements.

¹¹ <https://ssd.jpl.nasa.gov/horizons/>. This facility provides ephemerides for planets, small bodies, and satellites.

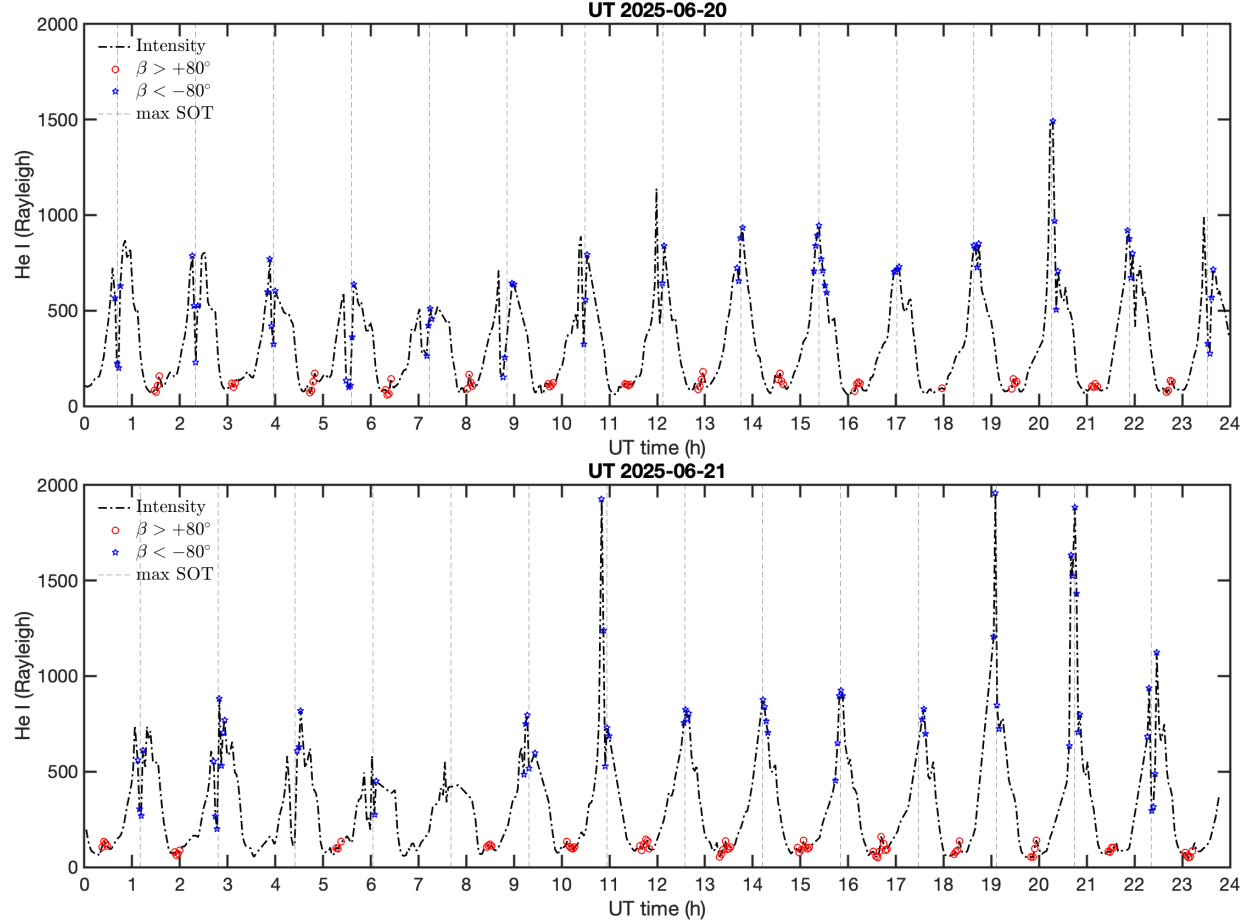


Figure 10. The strength of the He I $1.0833\text{ }\mu\text{m}$ line (in Rayleigh, R) over the course of two successive days (UT date noted in the title). The median uncertainty for the measurements is $4.4\text{ }R$. Note that the excursions to high values increased significantly on the second day. Observations at North and South Ecliptic poles ($|\beta| > 80^\circ$) are noted in the legend. The vertical lines mark time of maximum sun-observer-satellite angle (SOT).

Not only the concentration of helium increases in the wintry pole but also the supply of photoelectrons generated at the conjugate point, the bright summer pole, and transported to the wintry pole along magnetic field lines. As a result, the concentration of metastable is increased by an order of magnitude. Sutton et al. (2015) present a comprehensive model for the global distribution of helium at key junctures (solstices and equinoxes). Figure 2 of this paper is particularly informative, *We predict that SPHEREx will see strong $1.0833\text{ }\mu\text{m}$ emission at the north polar cap during the forthcoming northern winter season (December 2025).*

8.2. Solar Activity

Separately, the helium bulge phenomenon is sensitive to the activity of the sun. During solar minimum, the thermosphere is cooler (relative to that at solar maximum). As a result, the helium bulge is thicker at solar minimum relative to solar maximum. In addition, the metastable fraction is directly related to solar ac-

tivity (through an increase in the flux of energetic electrons, protons, and alpha particles, and an increase in the UV flux). Note that fast-moving solar alpha particles undergo successive charge exchange as they are slowed down by the neutrals in the upper atmosphere (Reasoner 1973).

Bearing this discussion in mind, I reviewed solar activity for June 20 and June 21, 2025. To start with, I note that the sun reached solar maximum late last year¹². The average F10.7cm radio flux¹³ during the month of June 2025 was 131 SFU, which should be contrasted with 70 SFU during solar minimum. Next, specifically on 20 June, the Sun emitted an X1.9 solar flare early in the (UT) morning of 20 June¹⁴.

¹² <https://www.swpc.noaa.gov/products/solar-cycle-progression>

¹³ <https://www.swpc.noaa.gov/products/solar-cycle-progression>

¹⁴ <https://science.nasa.gov/blogs/solar-cycle-25/2025/06/20/strong-flare-erupts-from-sun-5/>

From Figure 10 we see that there is significant variability during the passage across the SEP region. Some of this is due to SPHEREx pointing at different locations (all in the vicinity of the terminator plane). In fact, the models of Sutton et al. (2015) show significant spatial structures in the polar regions. A novel fish-eye lens imager with a narrow band centered on $1.0833\text{ }\mu\text{m}$, recently commissioned at the Poker Flat Research Range (65°N , 147°W ; Trondsen et al. 2024), show large-scale structures in the images (Meriwether et al. 2024).

Some of the variations could be due to an increase in metastable helium resulting from intermittent electron precipitation. This phenomenon has been seen in a 17-night winter campaign undertaken at the Kjell Henrichsen Observatory, Svalbard (78°N , 16°E) by Nishiyama et al. (2025). These authors performed spectral imaging observations covering the wavelength range $1.06\text{--}1.13\text{ }\mu\text{m}$ along with an incoherent scatter radar facility (EISCAT Svalbard Radar). The near-IR spectra are contaminated by strong and numerous OH lines. The authors modeled the spectra and infer emission from He I $1.0833\text{ }\mu\text{m}$. They find correlation between enhanced $1.0833\text{ }\mu\text{m}$ and precipitation of electrons into the thermosphere.

9. WAY FORWARD

The detection of strong He I $1.0833\text{ }\mu\text{m}$ emission from the thermosphere, while admittedly a hindrance for astronomers, nevertheless provides a new diagnostic tool for atmospheric scientists. The *data from just one orbit* of SPHEREx (see Figure 10) were sufficient to demonstrate the winter helium bulge phenomenon: a notably higher abundance of helium in the thermosphere above the wintry pole relative to that at the summer pole. Helium is nonreactive, so the explanation for the bulge is not connected with any photochemical reactions. The primary reason is large-scale circulation and atmospheric dynamics. The principal physical processes are advection (specifically, vertical winds) and molecular diffusion (recall that helium is lighter than oxygen and nitrogen). The source of energy for large-scale circulation is the heating of one hemisphere (during the summer appropriate to that hemisphere) relative to the other hemisphere; see Liu et al. (2014) for a recent review.

Bearing this summary in mind, we now highlight the possible contribution of SPHEREx to aeronomy. SPHEREx data, although confined to a band of sky close to the terminator plane, are global: a $3^\circ \times 360^\circ$ band along the terminator plane is covered in a single 97-minute orbit. Rigorous testing of global circulation models and their assumptions of key physical

processes can be undertaken by pitting the data provided by SPHEREx against the model predictions. Were SPHEREx to be funded to operate beyond the nominal 2-year prime phase, then the impact of solar activity on the helium bulge could be quantified.

Finally, as stressed by Sutton et al. (2015), the vertical distribution of helium has a direct effect on the orbital longevity of low-earth orbit (LEO) satellites. Given the increasing number of LEO satellites, it is of practical benefit to continue studying helium in the thermosphere. Most of the satellites are located below 650 km (e.g., Starlink is located at about 550 km, as is the case for Hubble Space Telescope and Swift Observatory). Earth observation satellites and defense satellites tend to be above 600 km.

Bearing this in mind, the reader should be aware that the column density of metastable helium atoms measured by SPHEREx is the column starting at 650 km and going to higher heights. In contrast, ground-based observations of He I emission yield the complete column density of metastable helium. The nightly monitoring during the winter season of Svalbard (for example Nishiyama et al. 2025) can be compared against SPHEREx data collected over about 15 passes per day. Coordinated lidar observations (e.g., Geach & Käfler 2025) would be particularly exciting, since these observations directly yield densities at the height of SPHEREx. In addition, adding electron density profile measurements with incoherent scatter radar observations may inform us of the origin of rapid brightening of the helium line.

One of the goals of SPHEREx is to use the technique of intensity mapping to investigate the early universe. This technique is a statistical technique that rests on the assumption that the non-astronomical signals are thoroughly understood. SPHEREx, being in a low-earth orbit, will suffer from the terrestrial foreground of which the most prominent feature is the He I $1.0833\text{ }\mu\text{m}$ line. As noted in the SPHEREx *Supplement* (cf. see also Figures 5 and 7) there will be fainter lines from atomic neutral and ionized species. These line features will vary, for a variety of reasons, including the activity of the sun. So, astronomers interested in the edge of the Universe may find themselves unwittingly in a position of precision modeling the very near foreground.

In §8.2 I noted that we are now past the solar maximum. So, in the future, as the sun quietens down, the emissions from the atmosphere can also be expected to decrease. It is anticipated that solar minimum will be reached in 2030. There is considerable value in operating SPHEREx through solar minimum.

ACKNOWLEDGMENTS

I thank Kishalay De (Columbia University) for a short tutorial on SPHEREx data and for several discussions. I am grateful to E. Sterl Phinney (Caltech) for patiently clarifying the definition of satellite inclination, Mike Werner (Jet Propulsion Laboratory, Pasadena) and Stefan Noll (German Aerospace Center, Bavaria, Germany) for detailed feedback on the manuscript, and Giulio Del Zanna (Cambridge University, Cambridge, UK) for supplying the model bound-free opacity table for metastable helium. I thank Sean Bryan (Arizona State University, Tempe, Arizona) and Jamie Bock (Caltech) for discussions regarding SPHEREx, Bruce Draine (Princeton University) for alerting me about the [Adams \(1949\)](#) paper, and Lynne Hillenbrand (Caltech) and Tom Greene (IPAC) for feedback.

I am grateful to John Meriwether (Clemson University, South Carolina; Center for Solar-Terrestrial Re-

search, New Jersey Institute of Technology), Takanori Nishiyama (National Institute of Polar Research, Tachikawa, Tokyo Prefecture, Japan), Christopher Geach (Deutsches Zentrum für Luft- und Raumfahrt, Oberpfaffenhofen, Bavaria, Germany) and Edwin Mierkiewicz (Embry-Riddle Aeronautical University, Daytona Beach, Florida) for patiently answering my questions about basic aeronomy terminology and clarifying various questions about helium in the thermosphere.

This publication makes use of data products from the Spectro-Photometer for the History of the Universe, Epoch of Reionization and Ices Explorer (SPHEREx), which is a joint project of the Jet Propulsion Laboratory and the California Institute of Technology, and is funded by the National Aeronautics and Space Administration.

REFERENCES

Abbas, A. H., Meng, X., Patil, R. S., et al. 2021, *PhRvA*, 103, 053317

Adams, W. S. 1949, *ApJ*, 109, 354

Anderson, K. S., & Kraft, R. P. 1969, *ApJ*, 158, 859

Birner, B., Severinghaus, J., Paplawsky, B., & Keeling, R. F. 2022, *Nature Geoscience*, 15, 346

Bishop, J., & Link, R. 1993, *Geophys. Res. Lett.*, 20, 1027

Bray, I., Burgess, A., Fursa, D. V., & Tully, J. A. 2000, *A&AS*, 146, 481

Catling, D. C., & Zahnle, K. J. 2009, *Scientific American*, 300, 36

Clausen, G., Gamlin, K., Agner, J. A., Schmutz, H., & Merkt, F. 2025, *PhRvA*, 111, 012817

Clayton, G. C., Geballe, T. R., & Zhang, W. 2013, *AJ*, 146, 23

Coddington, O. M., Richard, E. C., Harber, D., et al. 2021, *Geophys. Res. Lett.*, 48, e91709

—. 2023, *Earth and Space Science*, 10, e2022EA002637

Crill, B. P., Werner, M., Akeson, R., et al. 2020, in *Society of Photo-Optical Instrumentation Engineers (SPIE) Conference Series*, Vol. 11443, *Space Telescopes and Instrumentation 2020: Optical, Infrared, and Millimeter Wave*, ed. M. Lystrup & M. D. Perrin, 114430I

Crill, B. P., Bach, Y. P., Bryan, S. A., et al. 2025, *arXiv e-prints*, arXiv:2505.24856

Del Zanna, G., Storey, P. J., Badnell, N. R., & Andretta, V. 2020, *ApJ*, 898, 72

Draine, B. T. 2011, *Physics of the Interstellar and Intergalactic Medium* (Princeton University Press)

Drake, G. W. 1971, *PhRvA*, 3, 908

Drake, G. W., Victor, G. A., & Dalgarno, A. 1969, *Physical Review*, 180, 25

Drake, G. W. F., & Dalgarno, A. 1968, *ApJL*, 152, L121

Dupree, A. K., Sasselov, D. D., & Lester, J. B. 1992, *ApJL*, 387, L85

Dupree, A. K., Smith, G. H., & Strader, J. 2009, *AJ*, 138, 1485

Edwards, S., Fischer, W., Kwan, J., Hillenbrand, L., & Dupree, A. K. 2003, *ApJL*, 599, L41

Galazutdinov, G. A., & Krelowski, J. 2012, *MNRAS*, 422, 3457

Geach, C., & Kaifler, B. 2025, *Geophys. Res. Lett.*, 52, 2024GL112885

Goldberg, L. 1939, *ApJ*, 89, 673

Hall, D. N. B. 2011, in *American Astronomical Society Meeting Abstracts*, Vol. 217, *American Astronomical Society Meeting Abstracts #217*, 425.07

Harrison, A. W., & Cairns, C. D. 1969, *Planet. Space Sci.*, 17, 1213

Hodgman, S. S., Dall, R. G., Byron, L. J., et al. 2009, *PhRvL*, 103, 053002

Hung, T., Cenko, S. B., Roth, N., et al. 2019, *ApJ*, 879, 119

Hunten, D. M. 1982, *Planet. Space Sci.*, 30, 773

Indriolo, N., Hobbs, L. M., Hinkle, K. H., & McCall, B. J. 2009, *ApJ*, 703, 2131

Kaifler, B., Geach, C., Büdenbender, H. C., Mezger, A., & Rapp, M. 2022, *Nature Communications*, 13, 6042

Kockarts, G. 1973, *SSRv*, 14, 723

Liu, X., Wang, W., Thayer, J. P., et al. 2014, *Geophys. Res. Lett.*, 41, 6603

MacDonald, G. J. F. 1963, *Reviews of Geophysics and Space Physics*, 1, 305

Mathis, J. S. 1957, *ApJ*, 125, 318

Meftah, M., Damé, L., Bolsée, D., et al. 2018, *A&A*, 611, A1

Meriwether, J. W., Cooper, M. B., Gerrard, A. J., et al. 2024, in AGU Fall Meeting Abstracts, Vol. 2024, AGU Fall Meeting Abstracts, SA23B-2666

Moos, H. W., & Woodworth, J. R. 1973, *PhRvL*, 30, 775

Naito, H., Tajitsu, A., Arai, A., & Sadakane, K. 2013, *PASJ*, 65, 37

Nicolet, M. 1961, *J. Geophys. Res.*, 66, 2263

Nishiyama, T., Kagitani, M., Bag, T., et al. 2025, *Space Weather*, 23, e2024SW004161

Norcross, D. W. 1971, *Journal of Physics B Atomic Molecular Physics*, 4, 652

Oklopčić, A., & Hirata, C. M. 2018, *ApJL*, 855, L11

Pancharatnam, S. 1968, *Journal of Physics B Atomic Molecular Physics*, 1, 250

Patkóš, V., Yerokhin, V. A., & Pachucki, K. 2021, *PhRvA*, 103, 042809

Reasoner, D. L. 1973, *Reviews of Geophysics and Space Physics*, 11, 169

Rees, M. J., Sciama, D. W., & Stobbs, S. H. 1968, *Astrophys. Lett.*, 2, 243

Scherb, F. 1968, *ApJL*, 153, L55

Shefov, N. N. 1964, in *IAU Symposium*, Vol. 18, *Theoretical Interpretation of Upper Atmosphere Emission*, ed. D. R. Bates, 73

Spake, J. J., Sing, D. K., Evans, T. M., et al. 2018, *Nature*, 557, 68

Stebbins, R. F., Dunning, F. B., Tittel, F. K., & Rundel, R. D. 1973, *PhRvL*, 30, 815

Sutton, E. K., Thayer, J. P., Wang, W., et al. 2015, *Journal of Geophysical Research (Space Physics)*, 120, 6884

Thomas, K. F., Ou, Z., Henson, B. M., et al. 2023, *PhRvA*, 107, 033313

Trondsen, T. S., Meriwether, J., Unick, C., et al. 2024, *Journal of Astronomy and Space Sciences*, 41, 121

Ulrich, R. K., & Wood, B. C. 1981, *ApJ*, 244, 147

Waldrop, L. S., Kerr, R. B., González, S. A., et al. 2005, *Journal of Geophysical Research (Space Physics)*, 110, A08304

Woolley, R. V. D. R. 1934, *MNRAS*, 95, 101

Zhao, R., Liu, Z., Xue, X., et al. 2024, *Space Weather*, 22, e2024SW003977

Zirin, H. 1976, *ApJ*, 208, 414

Zirin, H., & Dietz, R. D. 1963, *ApJ*, 138, 664

APPENDIX

A. DATA ANALYSIS

Crill et al. (2020) is a good starting point for a reader to learn about the mission. As noted in §2 the fundamental reference to SPHEREx data is the “Explanatory Supplement”, provided by IRSA.

SPHEREx has a fixed observation pattern. The telescope is pointed in a fixed direction (in the general vicinity of the terminator plane) for a duration of about 113.6 s. The six detectors are readout, the telescope slews to the next programmed position, and the sequence is repeated. Here we focus on band 1 data.

The data product is a FITS file with seven extensions. Of relevance to us are the following: (1) a 2040×2040 -pixel “spectral image” (see Figure 1), (2) a 2040×2040 -pixel flag matrix, (3) a 2040×2040 -pixel variance matrix and (4) a 2040×2040 -pixel image of the zodiacal light as estimated from a preflight model. Some of these flags are generated at Level 1 (e.g., known non-functional/bad pixels) and others generated at Level 2 (e.g., charge spillover, cosmic rays, saturation, missing data, hot pixel, cold pixel, persistence, outlier). Passages through the South Atlantic Anomaly (SAA) are expected to suffer severely from cosmic-ray impacts. The reader should note that the flag with the key word “SOURCE” is applied for pixels assigned to a known source. So, fields at low Galactic latitudes will suffer from a high rate of rejection. In our analysis, given our focus on obtaining the sky spectrum, we rejected all pixels which were flagged. The histogram of the fraction of rejected pixels is summarized in Figure 11.

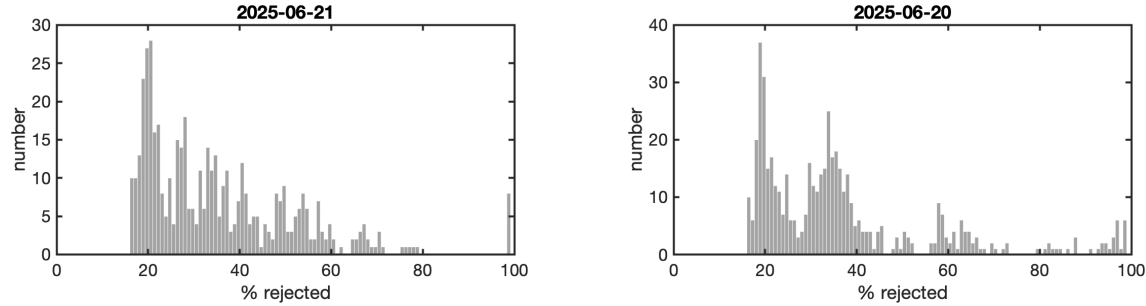


Figure 11. Histogram of percentage of rejected pixels. For each band 1 frame, the number of pixels which are flagged are counted. Dividing this by the total number of pixels yields the fraction of pixels flagged (x -axis). The y -axis is the number of band 1 image frames. The UT day for each data set is shown in the title.

Separately, IRSA supplies a matrix whose elements are the nominal wavelength associated with the corresponding pixel in the spectral image. I assigned these nominal wavelengths to each of the unflagged pixels of the spectral image. The pixels in the spectral image are then sorted by wavelength. The result is a 1-D spectrum. This spectrum is broken up into “sub-bands” of 701 pixels (“segment”). The median of each segment is obtained. The formal wavelength of each segment is the arithmetic mean of the wavelengths in each segment. The sky spectrum is the run of this median with wavelength. The He 1.0833 μm line integrated intensity was obtained by summing the spectrum over the wavelength range 1.054–1.106 μm (see Figure 3). The typical uncertainty in the integrated flux of the He I line is about 3×10^{-4} MJy ster $^{-1}$ μm . The zodiacal continuum is obtained as the mean value in the wavelength range [1.0, 1.2] μm .

The He I line has a small dip close to the peak (Figure 3). This feature is seen in almost all datasets. The feature seems to be an anticipated artifact of the system (see Figure 18 of Crill et al. 2025). The broad hump at 0.85 μm has been identified by the PI team as a leakage of the He I 1.0833 μm line (p. 16 of the *Supplement*).

B. LOMB-SCARGLE ANALYSIS

The Lomb-Scargle periodogram of the light curves shown in Figure 10 is shown in Figure 12. From this I infer an orbital period of 98.1 ± 1.7 minutes. According to *ISS Tracker*¹⁵ the current orbital period of SPHEREx is 97.69 minutes.

¹⁵ <https://isstracker.pl/en?satId=63182>

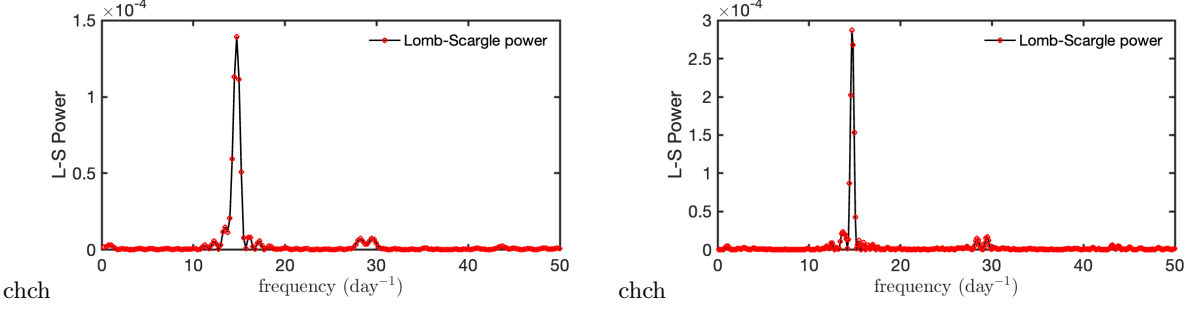


Figure 12. Lomb-Scargle periodogram of He I intensity (left: June 20, 2025; right: June 20–21, 2025). Notice the strong fundamental and even structure around the second harmonic. The inverse period from the left panel is $14.739 \pm 0.499 \text{ day}^{-1}$ (half-width at half maximum) and that from right panel is $14.683 \pm 0.251 \text{ day}^{-1}$. This corresponds to a period of $98.1 \pm 1.7 \text{ minutes}$.

C. PHYSICAL PROCESSES

C.1. Photoionization

A rough estimate of the bound-free photo-ionization cross-section can be obtained by assuming $\sigma_{\text{pi}}(\nu) \propto \nu^{-3}$ for $\nu > \nu_{\text{pi}}$ along with the normalization, $\int \sigma_{\text{pi}}(\nu) d\nu = \pi e^2 / (m_e c) f_{\text{pi}}$ (Woolley 1934). f_{pi} is computed using the Thomas-Reiche-Kuhn sum rule. From Table 1 we see that the sum of the oscillator strengths for all upward transition from the $1s2s \ ^3S_1$ state is 0.66. The oscillator strength of the decay of the 3S_1 to the ground state is negligible, -2.2×10^{-14} . Application of the sum rule to the $1s2s \ ^3S_1$ level then yields $f_{\text{pi}} = 0.34$. This approach has pedagogical value but is not expected to be accurate (especially at threshold energies). Norcross (1971) reported improved calculations. A more recent calculation is by N. Badnell which was used in Del Zanna et al. (2020).¹⁶

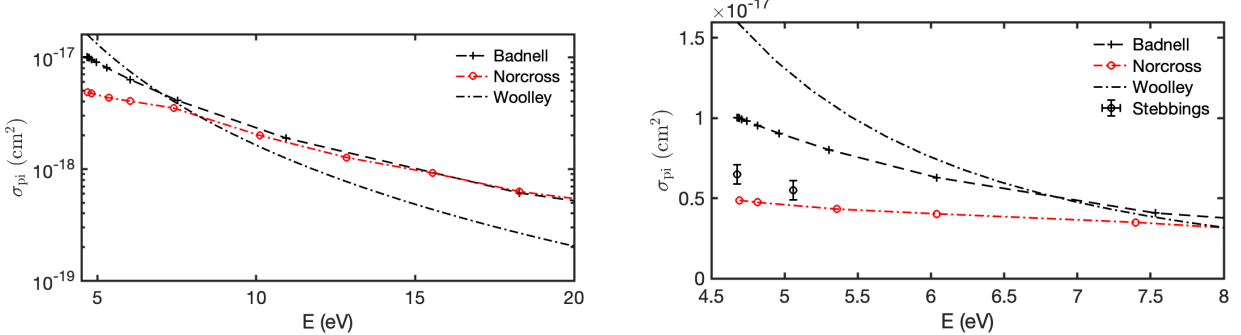


Figure 13. (Left): Run of bound-free cross-section (cm^2) for metastable helium with photon energy in eV. (Right): Zoom-in along with experimental points of Stebbings et al. (1973).

The three model calculations are summarized in the left panel of Figure 13. Surprisingly, there is only one experimental report on this important cross section (Stebbins et al. 1973). The measurements are close to threshold and lie between the two model calculations (right panel of Figure 13).

C.2. Other Processes

Recombination. The rate of di-electronic recombination is negligible relative to radiative recombination. The radiative recombination coefficients directly to the ground state ($1s^2$) and to all but the $1s^2$ level (ground state) are, respectively.

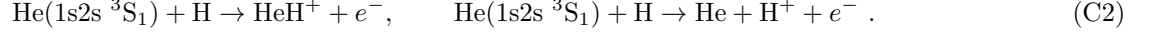
$$\alpha_{1s^2} = 1.54 \times 10^{-13} T_4^{-0.486} \text{ cm}^3 \text{ s}^{-1}, \quad \alpha_B = 2.72 \times 10^{-13} T_4^{-0.789} \text{ cm}^3 \text{ s}^{-1} \quad (\text{C1})$$

(§14.3 of Draine 2011). For the former, the free-bound photon emitted upon recombination, if absorbed locally, will result in another ionization. We assume that all ionizing photons escape from the thermosphere, in which case the

¹⁶ Del Zanna was kind enough to provide me the model cross-section data.

recombination coefficient is α , the sum of the two coefficients. The recombination rate per He^+ ion is αn_e where n_e is the electron density.

Collisional Ionization (Penning Ionization). A helium atom in the metastable state is 19.18 eV above the ground state. An encounter with a hydrogen atom can result in the ionization of the hydrogen and the liberation of an electron. Another channel, curiously, results in the formation of *helonium* (HeH^+ ; the very first molecule formed in the Universe):



Over a temperature range of 300 K to 4,500 K, the sum of the collisional ionization coefficient for the two reactions is $Q = 5 \times 10^{-10} \text{ cm}^3 \text{ s}^{-1}$.

Collisions with electrons. In astronomical atomic physics it is traditional to apply the formalism of electron-ion collisions to all collisions (see Chapter 2 of [Draine 2011](#)). The de-excitation rate coefficient, $\langle \sigma v \rangle_{ul}$, and its inverse are given by

$$\langle \sigma v \rangle_{ul} = \frac{h^2}{(2\pi m_e)^{3/2}} \frac{1}{(kT)^{1/2}} \frac{\Omega_{ul}(T)}{g_u} = \frac{8.629 \times 10^{-8}}{\sqrt{T_4}} \frac{\Omega_{ul}}{g_u} \text{ cm}^{-3} \text{ s}^{-1}, \quad \langle \sigma v \rangle_{lu} = \frac{g_u}{g_l} \sigma_{ul} e^{-E_{ul}/kT}$$

where u and l stand for upper and lower, g_u is the degeneracy of the upper level, Ω_{ul} is the dimensionless collisional strength, and E_{ul} is the energy difference between the lower and upper states, respectively. For electron-ion collisions Ω_{ul} has virtually no dependence on T .

Collisions that excite metastable helium to any level within the triplet family lead to a radiative cascade that will eventually bring the atom back to $1s2s \ ^3S_1$. In other words, such collisions do not change the density of metastable atoms. In the absence of a strong external source of light (e.g., the sun) excitations within the triplet family can be important (e.g., in planetary nebulae). In contrast, collisions which convert a metastable helium atom to para-helium will result in rapid radiative decay to the ground state. Given the modest electron temperatures, we only consider low energy (~ 1 eV) excitations which are summarized in Table 2.

[Bray et al. \(2000\)](#) present computed collisional strengths. The authors warn the reader “Because of the uncertainty that pseudo-resonances introduce into our cross sections at energies close to threshold, we limit the low temperature end of our tabulation to about 6,000 degrees.” We use the entries for 5,600 K. The collisions under discussion are electron & neutral. Thus, the collisional strength at, say, 3,000 K, will be lower. We reduce the strengths by 20% from that given in Table 2.

Table 2. Collisional de-excitations of He by electrons

| state | E_{ul} (eV) | Ω_{ul} |
|----------------------|---------------|---------------|
| $1s2p \ ^3P_{0,1,2}$ | 1.1438 | 15.1 |
| $1s2s \ ^1S_0$ | 0.7962 | 2.4 |
| $1s^2 \ ^1S_0$ | 19.8196 | 0.06 |

NOTE— For the first two entries the lower state is $1s2s \ ^3S_1$ while that for the third $1s2s \ ^3S_1$ is the upper state. The value of Ω_{ul} in column 3 is that at $T = 5,600$ K (from [Bray et al. 2000](#)).